

GriF: The New Three-dimensional Spectroscopic Mode of PUEO, the Canada-France-Hawaii Telescope Adaptive Optics Bonnette: First Observations in the Fabry-Pérot Scanning Mode

Y. CLÉNET,¹ E. LE COARER,² G. JONCAS,³ J.-L. BEUZIT,² D. ROUAN,¹ A. CHALABAEV,² P. RABOU,² R. ARSENAULT,⁴
C. DELAGE,¹ C. MARLOT,¹ P. VALLÉE,⁵ B. GRUNDSETH,⁶ J. THOMAS,⁶ T. FORVEILLE,⁶ O. LAI,⁶ AND F. LACOMBE¹

Received 2001 September 5; accepted 2002 January 30

ABSTRACT. Three-dimensional spectroscopy has the advantage of providing (quasi-) simultaneously both spatial and spectral information. Coupled to adaptive optics, it conjugates spectroscopic power with high angular resolution. GriF offers these capabilities in the near-infrared. As a new observing mode of KIR, the camera behind PUEO, the Canada-France-Hawaii Telescope adaptive optics bonnette, it provides images at the diffraction limit of the telescope in the *K* band. Spectroscopy at a resolution of 2000 is provided by a Fabry-Pérot interferometer coupled with a grism, cooled to limit the background. This setup offers a large multiplex gain by observing simultaneously up to five monochromatic images. This article first describes the instrument and the calibration procedures. Next, we demonstrate GriF performances from its first observations, obtained on the Orion molecular cloud OMC-1.

1. INTRODUCTION

Three-dimensional spectroscopy is a generic term for a large number of different instruments and techniques: Fabry-Pérot (FP) interferometers, Lyot variable filters, imaging Michelson interferometers, spectrometers coupled with a bundle of fibers in Argus mode or with image slicers or with microlens arrays, etc. However, they all lead to the same output data format, an (x, y, λ) cube. A classification scheme for all these techniques could be based on whether this cube is obtained in a single exposure or several exposures are necessary to cover the spectral and/or spatial domain. The former, which we consider to really deserve the integral field spectroscopy appellation, prevents any variation of the sky background or of the spatial/spectral instrumental response. The latter could be divided into

two classes depending on whether the data cube is made of successive exposures of the same region at different wavelengths (contiguous or not) or it is made of successive spectra of different regions (contiguous or not).

A large number of three-dimensional spectroscopic instruments are now in operation or under study, mainly in the visible. The interest in infrared three-dimensional spectroscopy arose with the improvement of the infrared detectors: larger format arrays, decreasing readout noise, and readout mode allowing one to window on selected areas. Despite the experience gained in adaptive optics techniques since the first astronomical dedicated system (COME-ON; Kern et al. 1990), only a few infrared three-dimensional spectroscopic instruments are—or will be—coupled to adaptive optics systems: 3D+ALPHA at the Calar Alto 3.5 m telescope (Davies et al. 2000), GraF at the La Silla 3.6 m telescope (Chalabaev et al. 1999), NIFS at Gemini North (McGregor et al. 1999), SINFONI at the ESO Very Large Telescope (Mengel et al. 2000), TEIFU at the William Herschel Telescope (Murray et al. 2000), and LUCIFER at the Large Binocular Telescope (Mandel et al. 2000).

GraF offers three-dimensional and long-slit spectroscopic capabilities to the ESO ADONIS adaptive optics system in the *J*, *H*, and *K* bands. It is composed of an FP interferometer and a grating, giving a spectral resolution of 7000 in the *K* band (up to 20,000 in the *J* band) in the three-dimensional mode. The optical components of GraF—the FP, the focal slit, and the grating—are all at room temperature, which makes it sensitive to the thermal background for wavelengths longer than 2 μm .

Observatoire de Meudon, Observatoire de Grenoble (which

¹ Observatoire de Paris, Département de Recherche Spatiale, 5 place Jules Janssen, F-92190 Meudon, France; yann.clenet@obspm.fr, daniel.rouan@obspm.fr, claude.delage@obspm.fr, claude.marlot@obspm.fr, francois.lacombe@obspm.fr.

² Observatoire de Grenoble, Laboratoire d'Astrophysique de l'Observatoire de Grenoble, B.P. 53, F-38041 Grenoble Cedex 09, France; etienne.lecoarer@obs.ujf-grenoble.fr, jean-luc.beuzit@obs.ujf-grenoble.fr, almas.chalabaev@obs.ujf-grenoble.fr, patrick.rabou@obs.ujf-grenoble.fr.

³ Université Laval, Québec, QC G1K 7P4, Canada; joncas@phy.ulaval.ca.

⁴ European Southern Observatory, Karl-Schwarzschild-Strasse 2, D-85748 Garching bei München, Germany; rarsenau@eso.org.

⁵ Université de Montréal, Département de Physique, CP 6128, Montréal, QC H3C 3J7, Canada; vallee@astro.umontreal.ca.

⁶ Canada-France-Hawaii Telescope Corporation, 68-1238 Mamalahoa Highway, Kamuela, HI 96743; grundseth@cfht.hawaii.edu, thomas@cfht.hawaii.edu, forveille@cfht.hawaii.edu, lai@cfht.hawaii.edu.

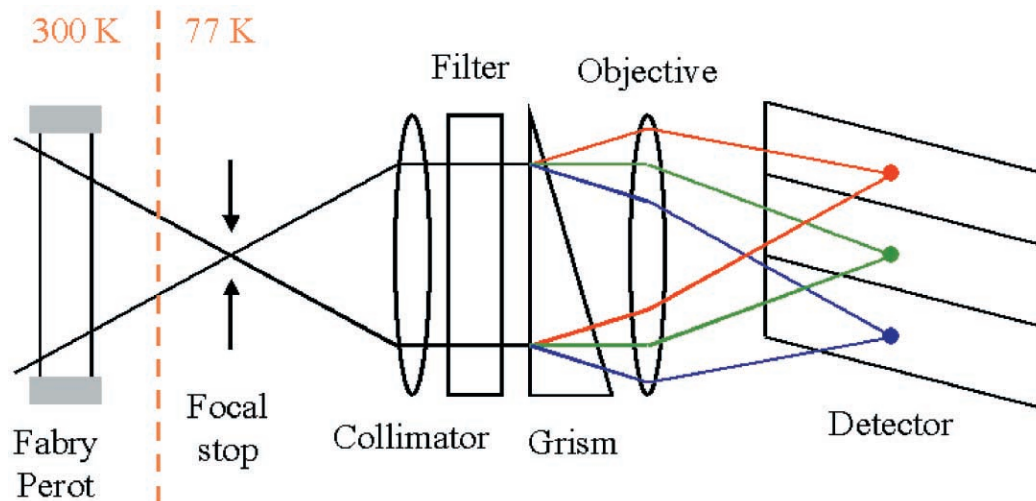


FIG. 1.—Optical setup of GriF. See text for description.

built GraF), and Université Laval, later joined by Université de Montréal, proposed to build for the Canada-France-Hawaii Telescope (CFHT) a new three-dimensional spectrograph named GriF and based on the GraF concept. Fed by the PUEO adaptive optics system (Rigaut et al. 1998), it avoids the GraF sensitivity drawback by placing all optical components but the FP in the liquid nitrogen-cooled cryostat of KIR, the near-infrared camera designed to be used at the focus of PUEO (Doyon et al. 1998). First observations with GriF were made in 2000 December, only in the FP scanning mode. The full setup should be available by the end of 2001.

In the first part of this article, we describe the instrument. In the second part, we present the FP adjustments and the data reduction process. The last part is dedicated to the first GriF

observations, obtained on the Orion molecular cloud, and to the inferred performances. Scientific results will be described in greater detail in a following paper.

2. GriF INSTRUMENTAL SETUP

As shown in Figure 1, GriF is mainly composed of three optical devices: the $f/20$ converging beam delivered by PUEO first passes through the FP interferometer, then a mask supported by a focal plane wheel, and finally a grism unit inserted in the KIR filter wheel.

2.1. The Fabry-Pérot Interferometer

2.1.1. The Fabry-Pérot Characteristics

An FP interferometer consists of two parallel flat mirrors whose inside surfaces partially reflect the incoming light. Multiple reflections in the cavity then create an interference pattern. To obtain a variable path difference, one accurately adjusts the distance between the two plates.

This interferometer was first described by Fabry & Pérot (1901), but it is only at the beginning of the 1980s that its use really grew in the astronomical community. This growth was partly due to a new system built by Queensgate Instruments (Pietraszewski 2001). Its operation is based on piezoelectric ceramic actuators and a highly stable servoloop, which made possible the accurate control of the relative position of the mirrors.

The GriF interferometer is a Queensgate ET50WF Fabry-Pérot, designed according to our specifications to work in both H and K bands. The plates are made of water-free fused silica. Their reflection coefficient is greater than 97% between 1.5 and 2.5 μm (Fig. 2). The nominal gap between the plates is 31.5 μm . The plate flatness is better than $\lambda/170$ at 1523 nm.

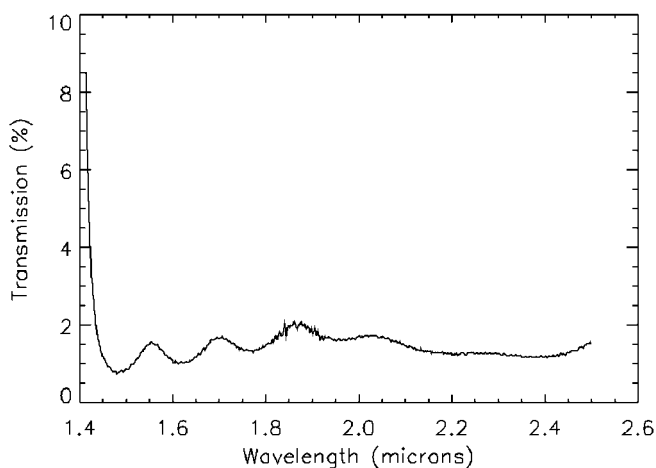


FIG. 2.—Transmittance—profile of the GriF interferometer high-reflectivity coating curve.

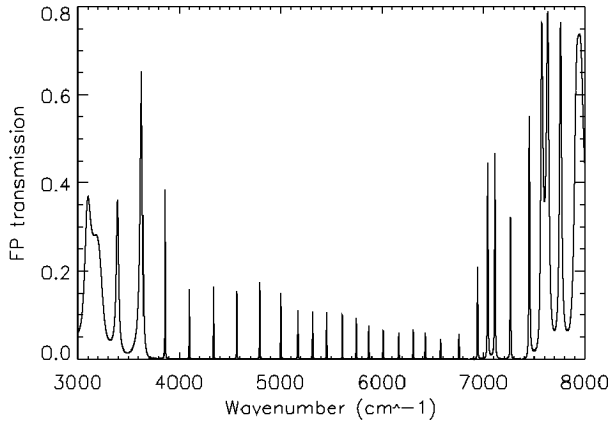


FIG. 3.—FTS spectrum of the GriF interferometer.

The theoretical intensity transmitted by the interferometer is given by the following formula:

$$I(\lambda) = \frac{1}{1 + F(\lambda) \sin^2 [\psi(\lambda/2)]} \left(1 - \frac{a}{1 - R}\right)^2,$$

where λ is the observed wavelength, R the reflection coefficient of the plates, a the absorption coefficient of the plates ($a \approx 0.002$), F a coefficient defined by

$$F = \frac{4R}{(1 - R)^2},$$

and ψ the phase:

$$\psi(\lambda) = \frac{4\pi\mu e \cos(\theta)}{\lambda}.$$

In the last formula, μ is the refractive index of the medium within the gap ($\mu \approx 1$), θ the angle from the optical axis, and e the gap.

If the gap is set in order to have an on-axis ($\theta = 0$) destructive interference, $(p + \frac{1}{2})\lambda = 2e$, where p is an integer. The angle θ_1 for which a constructive interference occurs is given by $p\lambda = 2e \cos(\theta_1)$. Then $\cos(\theta_1) = 1 - \lambda/4e$. For a nominal gap of $31.5 \mu\text{m}$ at $2.2 \mu\text{m}$, $\theta_1 = 10^\circ 7'$. The PUEO output pupil ($0^\circ 93'$) is then contained in a much smaller surface than the one circumscribed by the first ring of the FP.

An analysis of the interferometer was performed with a Fourier transform spectrograph (FTS). The FP was illuminated by a collimated beam produced by a halogen lamp; the output was then fed into the FTS. Figure 3 presents the obtained spectrum, divided by the spectrum of the halogen source.

The intensity peaks' variation in Figure 3 must not be interpreted as absorption within the FP but is due to the imperfect alignment of the interferometer during the experiment. Since

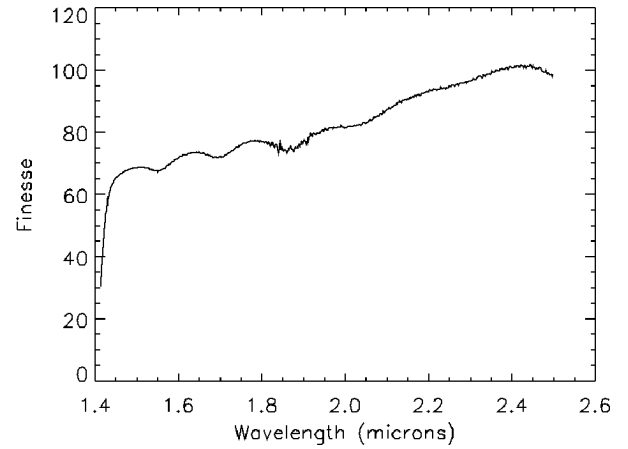


FIG. 4.—GriF FP finesse computed according to the transmittance profile (Fig. 2).

the coating has a very high reflectivity, any departure from parallelism has a strong effect on the peak transmission.

The resulting finesse N_t of the FP is given by

$$N_t = \left(\frac{1}{N_r^2} + \frac{1}{N_d^2} + \frac{1}{N_i^2} \right)^{-1/2},$$

where

- $N_r = (\pi\sqrt{F})/2$ is the reflective (theoretical) finesse;
- $N_d = (170/1.523)(\lambda/2)$ is the defect finesse, related to the plate flatness (better than $\lambda/170$ at $1.523 \mu\text{m}$); and
- $N_i = \lambda/2\Delta e$ is the aperture finesse. In a converging beam, the range of incident angle on the FP plates is equivalent to a gap between variable plates that degrades the finesse. In the $f/20$ PUEO output beam, the maximum incident angle is $\alpha = \arctan(0.5/20)$ and the equivalent gap is given by $\Delta e = e/\cos \alpha - e = 9.84 \times 10^{-3} \mu\text{m}$.

From the transmittance presented in Figure 2, one can compute the three finesse profiles (N_r , N_d , and N_i) as a function of wavelength and draw the profile of the total finesse (Fig. 4).

Knowing that the finesse is also equal to the ratio between the separation of two successive peaks and their widths, one can check this parameter by scanning a calibrated line with two successive FP orders. During the first GriF run, scans of the $2.06163 \mu\text{m}$ argon line were made (Fig. 5). Because the instrumental profile is non-Gaussian and wider than the width of the argon line, Lorentzian fits have been made of these profiles from which a finesse of 104 was derived. Hence, the instrumental resolution of the instrument is around $1.014 \times 10^{-3} \mu\text{m}$, which leads to a spectral resolution $\lambda/\delta\lambda = 2030$.

One should also note that our optical configuration is particularly advantageous regarding ghost formation. The main sources of ghosts are placed after the FP in the optical path:

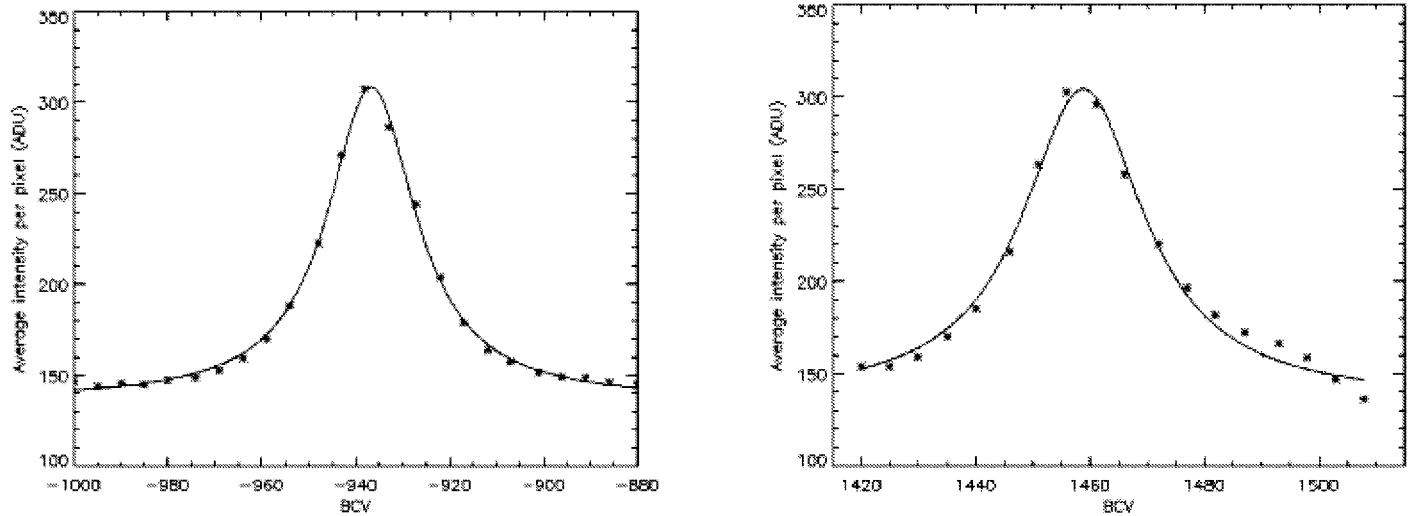


FIG. 5.—Profiles of the $2.06163 \mu\text{m}$ argon line, scanned with the GriF interferometer in two successive orders. On the X-axis are reported the BCVs (see § 3.1.1 for a definition) sent to the FP controller. On the Y-axis are reported the mean values of each step image of the scan, expressed in ADU. Crosses represent discrete values. Lines represent the Lorentzian fits. One can note the bump on the right wing of the second profile, which is certainly due to another line observed at a superior order.

the grism, the lenses, and the filter or the detector. This way the parasitic reflections coming from these optical devices are located in the wavelength domain where the FP transmits 100% of the light; hence, no secondary reflections return back toward the detector.

2.1.2. The Fabry-Pérot Interface

The interferometer and its support are located in an interface between PUEO and KIR that usually aims at adjusting the

position of the PUEO output focus. This spacer also contains the shutter that controls the exposure time. Even though the spacer is not cooled, the thermal background introduced by the interferometer is very low as it is seen as a mirror at a temperature around 0°C (the temperature inside the dome).

Designed at the Observatoire de Meudon and manufactured at the Université Laval, the GriF interface (Fig. 6) corrects half of the defocusing induced by the interferometer in the beam (16.4 mm) thanks to an appropriate height. The second half is taken in charge by the adaptive optics system as a static aberration. In this configuration, this interface can be used when the FP is either in or out of the beam: in each case the adaptive optics system has to correct a defocus of 8.2 mm.

A rail system allows one to manually insert (remove) the FP in (from) the beam. The stability of the two positions is ensured thanks to mechanical stops.

To prevent from any change in humidity or temperature, a dry nitrogen supply is ensured between the plates of the GriF FP.

A drawback of the shutter used in the former KIR spacer was its inability to stay in an opened position without being powered. This resulted in the heating of the solenoid that controls the shutter position and thus in the alteration of the image quality. This effect was not measurable in the former KIR setup but may affect GriF observations for at least three reasons:

- the GriF shutter has a larger diameter and thus a bigger solenoid with a more important heating power;
- the typical exposure time for GriF is longer than for KIR in its classical observing mode since the spectral resolution of broadband and narrowband filters is much smaller than for the FP; and

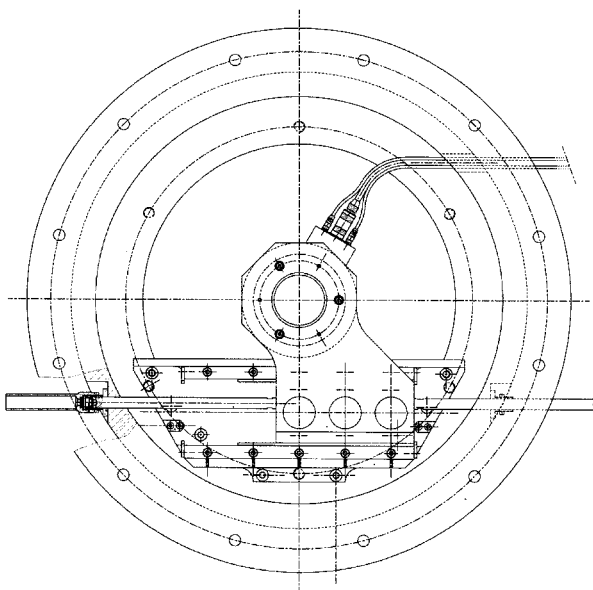


FIG. 6.—General drawing of the GriF spacer.

TABLE 1
GRISM PARAMETERS

Parameter	Value
Direct vision wavelength (μm)	2.1
Groove number (mm^{-1})	164
Ruled area (mm^2)	9×15
Blaze angle (maximum transmission) (deg)	14.5
Maximum transmission (%)	57

- the FP, which filters the telescope and atmosphere thermal emission between the transmission orders, does not cut the thermal background induced by the solenoid since the latter is located between the FP and the detector.

To get rid of these disadvantages, the opening and closing of the GriF shutter are controlled by a holding electromagnet that gives two stable unpowered positions when it is coupled with a spring. The opening of the shutter is done by sending a short pulse to the electromagnet. This position is held by magnetic locking. By sending another pulse, with an inverse polarity with respect to the first one, the shutter returns to its closed position.

2.2. The Grism Unit

Only a few years after his first proposition for a “new form of interferometer” (Fabry & Pérot 1901), Fabry described the interest of separating the transmitted orders of an FP interferometer (Fabry 1905). Without this disperser, the image recorded on the detector would be the superposition of the quasi-monochromatic images transmitted by the interferometer.

The GriF disperser is a grism that acts like a transmitting blazed spectrograph and is located inside the KIR cryostat to cut back the thermal background, an inconvenience encountered with GraF. A grism permits a more compact configuration than a grating. However, at a given refractive index, the dispersion for a grism is lower. Therefore, the grism has to be manufactured with a high refractive index in the working wavelength domain. In the near-infrared, a common optical material for grisms is the KRS-5 monocrystal (or thallium bromo-iodide, TlBr-TII). Its refractive index is 2.39 at $2 \mu\text{m}$ at 300 K. The major inconvenience of this material is its fragility under mechanical constraints, and special caution must be taken for its support in the cryostat. The GriF grism is direct-ruled, which

prevents delamination during thermal cycling and internal reflections that could have occurred with a replicated grism. Our grism works in only the *K* band. Since our FP was designed for both *H* and *K* bands, *H*-band observations are possible provided the purchase of a dedicated grism.

The grism was manufactured by Karl Zeiss, Jena. Table 1 summarizes the grism’s parameters.

To measure the wave front quality coming out of the grism, the latter was illuminated by a He-Ne laser ($\lambda = 632.8 \text{ nm}$), and the lowest order spot (the brightest) was analyzed with a Hartmann wave front sensor. Results for different laser beam positions on the front side of the grism are presented in Table 2. If the 0° astigmatism aberration is not taken into account, the wave front errors are better than $\lambda/49$ rms at $2.2 \mu\text{m}$. If this aberration is included, $\lambda/3.3$ rms at $2.2 \mu\text{m}$ is obtained. If we consider only the difference from the mean value of this aberration (i.e., 550 nm), errors better than $\lambda/18$ rms at $2.2 \mu\text{m}$ are derived. The mean 0° astigmatism aberration is probably due to the anamorphism of the laser beam. The astigmatism will be corrected by the adaptive optics system as a static aberration.

The beam coming out from the FP is converging. Its collimation is performed by a first lens introduced in front of the grism. The second lens is located behind the grism and is used as a camera lens.

A filter is located between the first lens and the grism to the transmission of only the *K*-band FP orders. Its bandpass covers $1.98\text{--}2.50 \mu\text{m}$ (wavelengths corresponding to 50% transmittance at 77 K; Fig. 7). The bandpass has been widened with respect to the usual *K*-band filter in order to benefit from a larger part of the *K*-band atmospheric window and to be able to scan more redshifted extragalactic lines.

Filter and lens parameters are summarized in Table 3.

These four optical parts (collimating lens, filter, grism, and imaging lens) are assembled in a cell, located in the KIR filter wheel. It is selected like a filter, allowing the use of the classical KIR observing mode. Designed and manufactured by the Université de Montréal, this cell is inserted in a 1 inch filter wheel slot. The maximum 7 mN-m torque induced by the weight of this cell (around 36 g, compared to 15 g for a usual filter cell) does not alter the balance of the filter wheel.

Spot diagrams of the complete optical system are presented in Figure 8. At this time, the grism subsystem has not yet been

TABLE 2
MEASURED GRISM WAVE FRONT ERRORS (RMS)

Errors Computed	Position 1 (nm)	Position 2 (nm)	Position 3 (nm)	Position 4 (nm)	Position 5 (nm)	Position 6 (nm)
Without astigmatism aberrations	36.4	29.5	27.8	44.8	19.8	33.9
Without the 0° astigmatism aberration	44.1	39.6	28.7	45.0	19.9	35
With astigmatism aberrations	575	565	557	661	429	520
With the difference from the mean 0° astigmatism aberration	49.7	42.0	29.3	118.8	123.6	46.1

NOTE.—Tilt and defocus aberrations have not been taken into account for the computation of the wave front errors.

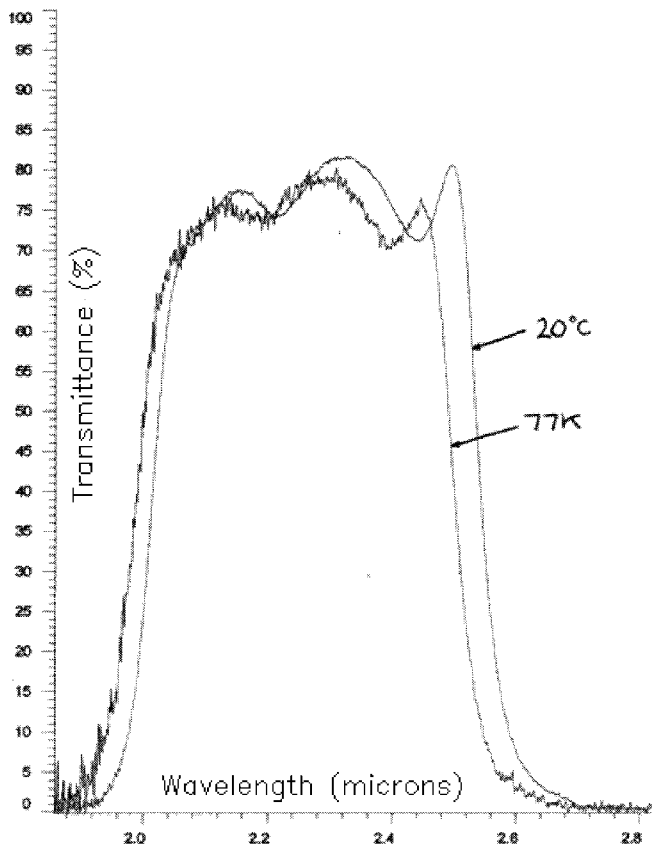


FIG. 7.—GriF filter transmittance profiles.

tested on the sky. A following article will describe its performance after future tests.

2.3. The Focal Plane Wheel

Without a mask in the KIR focal plane, the monochromatic images transmitted by the FP would overlap. A wheel has been designed and manufactured by the Observatoire de Paris to support the masks. Because of severe space limitations, a compact design has been realized according to the principle of a Maltese cross: a single mechanical element drives the wheel and ensures its positioning at the same time (Fig. 9). The indexation of the positions is secured by two microswitches. A first one gives the “zero position,” and the second one is triggered at each position of the Maltese cross.

There are 18 wheel positions, enabling the use of eight different masks and a clear circular aperture. The latter permits the KIR classical imaging mode. Since the role of the apertures in the GriF mode is to prevent the overlapping of the images in different orders, its width along the grism dispersion direction, expressed in wavelength, must not be larger than the distance between the FP orders (also called free spectral range). However, this free spectral range varies with the wavelength: from 80 nm at 2.0 μm to 150 nm at 2.4 μm . On the other hand,

TABLE 3
PARAMETERS OF THE GRIF LENSES AND FILTER

Parameter	Collimating Lens	Imaging Lens	Filter
Material	BaF ₂	BaF ₂	Silica
Type	Plano-convex	Plano-concave	Biplan
Diameter (mm)	12.00	12.00	12.66
First radius (mm)	∞	52.33	...
Second radius (mm)	45.30	∞	...
Central thickness (mm)	1.5	1.0	1.49

the wider the aperture, the larger the field of view. Therefore, with a spectral domain as large as the one provided by GriF, a single aperture cannot satisfy both requirements. Hence, two apertures were retained (Fig. 10). The narrower was chosen to keep uncontaminated almost all GriF windows in the *K* band, in particular for the He I line at 2.06 μm . Its corresponding field of view is 4".3. The other one has the largest possible field of view (5".9) with no contamination at the wavelength of the CO 2.3 μm band.

The wheel also supports three different apertures for the long-slit spectroscopy mode, when the FP is out of the beam. One has a corresponding slit width on the sky of 0".15 and allows the highest spectral resolution for point-source objects. Two other apertures (with fields of view of 0".2 and 0".4) are foreseen for fainter objects, which may have a smaller Strehl ratio.

All five apertures have a length that is limited by the size of the detector (i.e., 36" on KIR). The last three apertures of the wheel will be filled by coronagraphic masks.

2.4. Calibration Lamps

As explained in § 3, lamps emitting reference lines and uniform white light are needed to obtain wavelength and flat-field calibrations.

For this purpose, GriF uses the CFHT Cassegrain calibration unit, called Gumball. This system, originally designed and fabricated by the Observatoire de Marseille as a visible spectral calibration unit for the CFHT MOS/SIS spectrograph, has been upgraded to match the requirements of new CFHT instruments such as the Adaptive Optics Bonnette, OASIS, or CFHT-IR. Now Gumball is equipped with two argon lamps, two neon lamps, two halogen lamps, and two mercury lamps that cover our needs.

2.5. GriF Observing Modes

Once all optical and mechanical parts are installed, GriF will offer several new observing modes in addition to the KIR classical imaging mode:

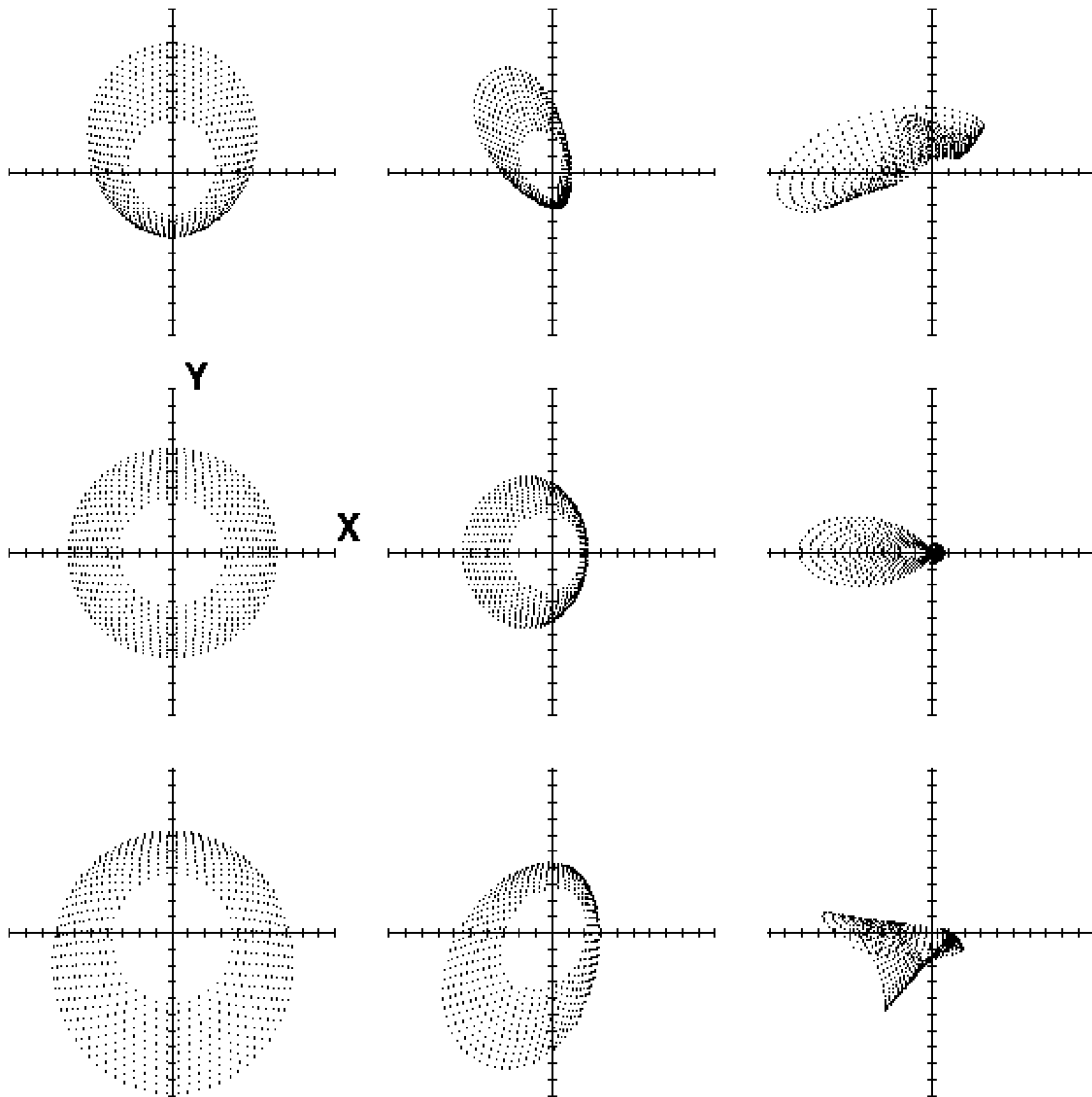


FIG. 8.—GriF *K*-band spot diagrams. *X*- and *Y*-axis scales are both 0.0002 mm by ticks. Pupil dimensions along *X*- and *Y*-axes are both 40 mm. The upper line corresponds to 1.961 μm , the middle one to 2.2577 μm , and the lower one to 2.532 μm .

- *Long-slit mode*: only the grism and a slit are selected.
- *Static line imaging mode*: a mask, the grism, and the FP are selected. In this case, the FP is used at a fixed gap as a high-resolution filter. Five quasi-monochromatic images will be displayed in a single image, allowing one to observe simultaneously one line of interest and the continuum.
- *FP scanning mode*: only the FP is selected, and a line is scanned by changing the FP gap.
- *GriF scanning mode*: this is the conjugation of the two preceding modes. The grism, the FP, and a mask are selected, giving several images on the detector. The interferometer's gap is changed step by step.
- *Coronagraphic mode*: this is available by placing a Lyot mask on the focal plane wheel.

3. CALIBRATIONS AND DATA REDUCTION

3.1. The Fabry-Pérot Adjustments

3.1.1. Controlling the Fabry-Pérot Plates' Interspacing

The GriF interferometer control is in the hands of the Queensgate CS 100 controller owned by CFHT. It servo-stabilizes the parallelism of the mirrors and the cavity spacing of the interferometer. Two channels (*X* and *Y*) are dedicated to the parallelism control and a last one (*Z*) to the spacing between the plates. All three act on piezoelectric devices. The control can be done manually or via a computer-controlled interface bus that sends binary control values (BCVs) to each channel (*X*, *Y*, and *Z*). The following paragraphs describe the control of the gap (*Z*) for the GriF FP. In the next section (§ 3.1.2), we will describe the parallelism adjustment.

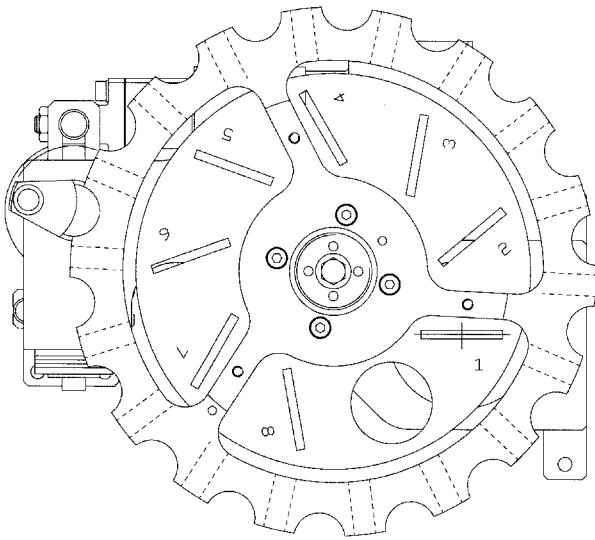


FIG. 9.—Top view of the GriF focal plane wheel.

The interference orders of a theoretical FP spectrum should be separated by a constant wavenumber value. The reader will note that this is not the case for the GriF interferometer FTS spectrum as shown in Figure 3. Usually observed in FP, these irregularities are amplified for the GriF FP because the depth of the dielectric coating is comparable to the gap between the mirror plates (around $31 \mu\text{m}$).

This irregular effect on the positions of the FP orders translates into difficulties in controlling the gap with respect to the desired transmitted wavelengths. The following paragraphs describe the method used to take into account these irregularities.

We can assume that, at any wavelength λ , a gap change of $\Delta e = +\lambda/2$ will increase the order number by 1. In order to adjust the interferometer at a requested λ , we may find which Δe is necessary to put the closest order at λ . For this purpose, a relative gap curve $\Delta e(\lambda)$ is computed based on the peaks' wavelengths measured in Figure 3. For each successive order, we increase $\Delta e(\lambda)$ by $\lambda_i/2$: for any λ_i , a gap increase of $\lambda_i/2$ moves the order i at λ_{i+1} . This discrete function can be interpolated by a cubic spline method (Fig. 11). Then, the FP

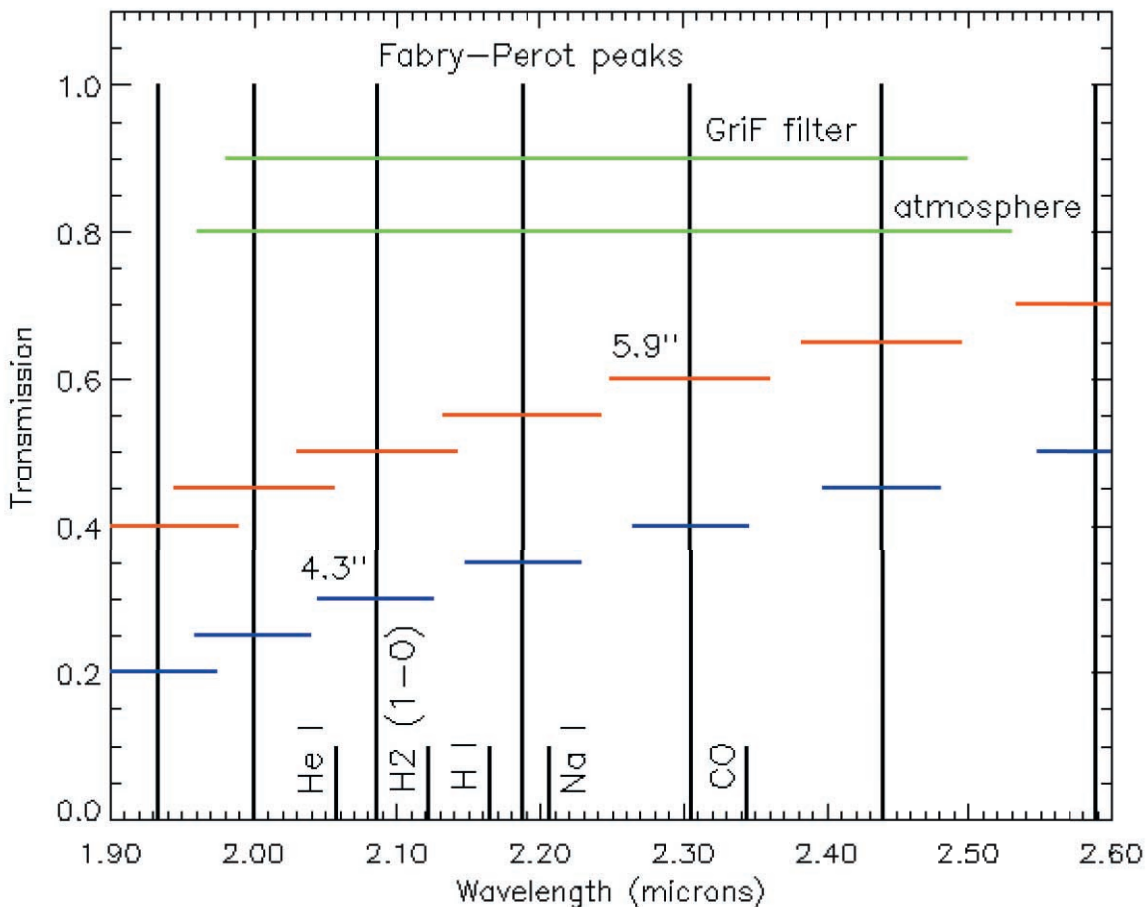


FIG. 10.—Chosen focal apertures with the FP transmission peaks. The atmospheric *K* band is given with the spectral domain covered by GriF (wavelengths with a filter transmission greater than 50%). A selection of useful astronomical lines is also indicated.

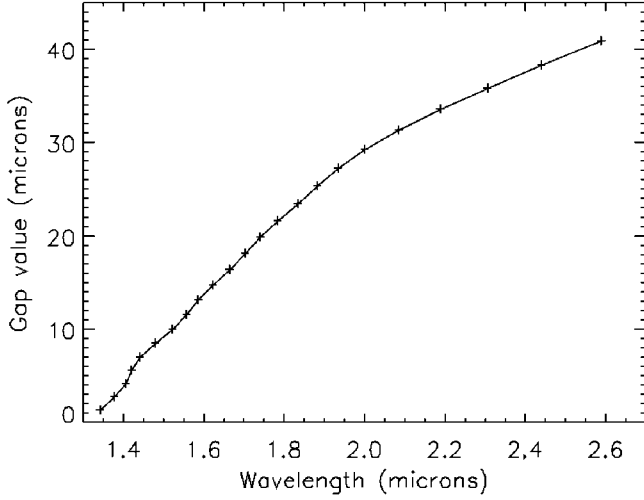


FIG. 11.—The gap curve. Crosses are the discrete values. See text.

adjustment procedure consists in finding the closest λ_i and applying on the interferometer the gap difference found by reading the curve at λ and λ_i . For any wavelength value, the corresponding gap change applied by the controller is given by $\delta e(\lambda) = \Delta e(\lambda) - \Delta e(\lambda_i)$, where λ_i is the closest order in the FTS spectrum. Note that, inversely, wavelength can also be a function of gap [$\lambda(\Delta e)$] and be retrieved from a given δe in the inverse curve.

The CS 100 controller permits the interferometer gap to be scanned over $\pm 2 \mu\text{m}$ around a zero position for which the FTS spectrum has been obtained. When the controller is not exactly centered on the zero position given by the FTS spectrum, it is possible to adjust the orders' wavelength by scanning a well-known spectral line (argon at $2.06163 \mu\text{m}$ for example). The obtained gap value is compared to the value given in the curve above. The difference between these two values is then used to compute each order wavelength: $\delta s = \delta e(\text{Ar } 2.06163 \mu\text{m}) - \delta e_{\text{obs}}(\text{Ar } 2.06163 \mu\text{m})$; then $\lambda'_i = \lambda_i - \lambda(\delta s)$, and a new gap curve can be built.

3.1.2. The Fabry-Pérot Parallelism

A first rough adjustment of the parallelism is made manually and by eye. A lamp emitting a spectral line in the visible, observed through the interferometer, produces a ring pattern. By moving one's eyes along the X- or the Y-axis, this pattern will contract, or expand, if the plates are not parallel. This effect is corrected by setting appropriately the X- and Y-values on the CS 100 front panel.

A second remote adjustment is necessary because of the high finesse of the GriF FP. A “phase map,” which gives the wavelength variation across the field, can be built by scanning a calibrated line. This three-dimensional map can be well approximated by a parabolic function: $I(x, y) = a + b(x - x_c)^2 + c(y - y_c)^2$. If the FP is well aligned, the center

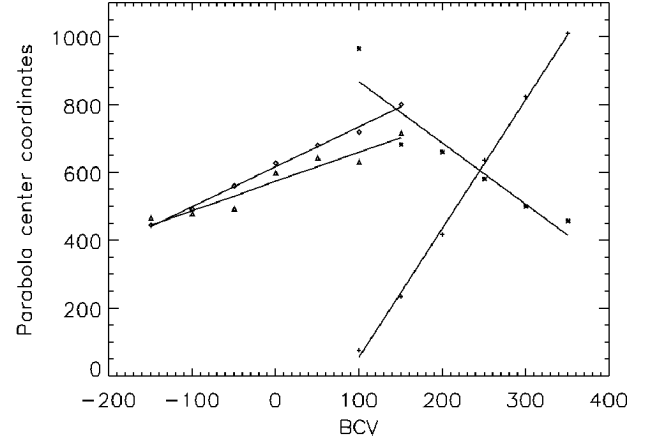


FIG. 12.—Evolution of the parabola center position on the detector with varying BCV. Discrete points are for the coordinates. Lines are linear fits of these coordinates' variation. The crosses are for the variation of the X-coordinate as a function of BCV_y . The asterisks are for the variation of the Y-coordinate as a function of BCV_y . The diamonds are for the variation of the X-coordinate as a function of BCV_x . The triangles are for the variation of the Y-coordinate as a function of BCV_x .

of this function should be coincident with the so-called hot spot of PUEO, which is the location of an observed star when the wave front sensor is *on-axis*. As shown on Figure 12, the center of the parabola has a position, given by its coordinates (x_c, y_c) , which depends on the parallelism adjustments of the interferometer. Linear fits of these coordinates as functions of BCV give the following relations:

$$\begin{pmatrix} x_c \\ y_c \end{pmatrix} = \begin{pmatrix} 3.8033 & 1.1784 \\ -1.8108 & 0.85703 \end{pmatrix} \begin{pmatrix} \text{BCV}_x \\ \text{BCV}_y \end{pmatrix},$$

and by a simple inversion:

$$\begin{pmatrix} \text{BCV}_x \\ \text{BCV}_y \end{pmatrix} = \begin{pmatrix} 0.15890 & -0.21848 \\ 0.33575 & 0.70519 \end{pmatrix} \begin{pmatrix} x_c \\ y_c \end{pmatrix}.$$

Hence, the parallelism of the interferometer can be set at any time by making a single scan of the calibrated line at given BCV values on X and Y channels (say BCV_{x_0} and BCV_{y_0}). Then, the BCV values corresponding to the parallelism adjustment are given by

$$\begin{pmatrix} \text{BCV}_{x_0} - \text{BCV}_x \\ \text{BCV}_{y_0} - \text{BCV}_y \end{pmatrix} = \begin{pmatrix} 0.15890 & -0.21848 \\ 0.33575 & 0.70519 \end{pmatrix} \begin{pmatrix} x_c - x_h \\ y_c - y_h \end{pmatrix},$$

where x_c and y_c are the measured coordinates of the parabola center and x_h and y_h the coordinates of the PUEO hot spot.

3.2. Data Reduction

This paragraph is dedicated to the calibration and data reduction procedures to be followed to end with calibrated data.

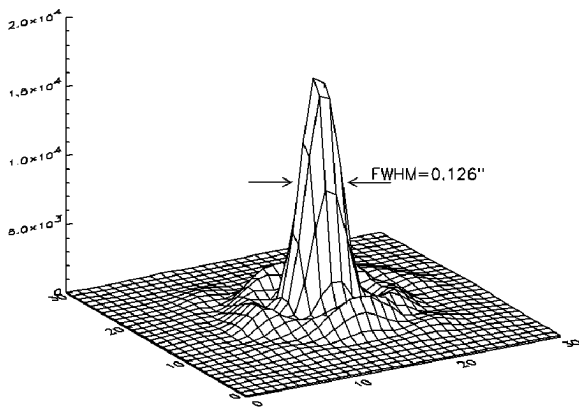


FIG. 13.—Profile of BS 6629 obtained with GriF at $2.059 \mu\text{m}$. Vertical units are arbitrary. The achieved spatial resolution is $0''.126$.

A manual giving more details and practical information is available for observers at CFHT.

3.2.1. Dark and Bias Subtraction

A dark map is a closed-shutter time-dependent exposure that contains information on

1. the bias, which includes a constant offset (100 ADU for KIR), added to ensure positive pixel values, and the internal response structure of the detector; and
2. the dark current of the detector ($0.15 e^- s^{-1}$ for KIR), which depends on the integration time.

Scientific exposures can be corrected for the bias and the dark current by subtracting this dark map.

3.2.2. Flat-Field Correction

Each pixel of the detector has its own sensitivity, mainly because of the nonuniform response of the optics. To correct this effect, the object frames must be divided by a flat field. In classical imaging, this flat-field frame is built by observing the sky at twilight or a uniform illumination of the dome.

When using an FP, one obtains the flat field, commonly called a white-light cube, by reproducing the same scan as on the scientific object, while observing a uniform field. Considering the resolution of the interferometer, the observation of the sky at twilight would be too long, hence the use of a white halogen lamp. Another reason to avoid twilight observations for the FP flat field is its sensitivity to the orientation of the telescope. Then, in addition to the object cube, a second cube is built at the same wavelengths (or BCV) just before or just after the former. The flat-field-corrected cube is constructed by dividing the two cubes plane by plane.

For GriF, with the two Gumball halogen lamps on, the appropriate exposure time for each step of the white-light cube is 10 s. Including the readout time and the Gumball setup, a

typical white-lamp scan (with eight steps) lasts between 5 and 10 minutes.

During our first run in 2000 December, a correct flat-field calibration procedure was not used, and white-lamp exposures were not available for all the wavelengths observed on OMC-1. However, the fringe pattern produced during a flat-field scan is periodic, and we managed to correctly flat-field all the scientific images.

3.2.3. Bad Pixel Correction

A dead pixel map can be obtained from a classical flat field, by selecting pixels with gain values outside a well-selected range ($[0.5, 2]$, for example). Often, additional bad pixels must be corrected on each scientific image. The selection of these additional bad pixels can be achieved from their statistical deviations compared to their neighbors.

3.2.4. Spatial Resolution and Image Recentering

The GriF spatial resolution was tested during a technical night by observing a bright star, BS 6629 ($m_V = 3.75$), with two density filters for the wave front sensing, leading to an equivalent magnitude $m_V = 8.75$. Figure 13 shows its profile at $2.059 \mu\text{m}$, obtained during a scan of the $2.06 \mu\text{m}$ He emission line. The achieved spatial resolution ($\text{FWHM} = 0''.126$) is very near the diffraction limit ($0''.118$), demonstrating that GriF FP does not degrade the PUEO performance in terms of image quality.

A well-known phenomenon may affect the spatial resolution: the differential refraction of the atmosphere. Indeed, wave front sensing and scientific observations are not performed at the same wavelength. Thus, while the adaptive optics system keeps the reference star position locked in the visible, the infrared field drifts with the changing air mass. Based on formulae from Filippenko (1982) and Mauna Kea atmospheric conditions from Cohen & Cromer (1988), Figure 14 gives the GriF maximum exposure time in order to have a drift lower than one-fourth of the diffraction limit at $2.12 \mu\text{m}$. We can see that except for extreme cases, differential refraction will not degrade the spatial resolution during an exposure.

However, in addition to telescope and instrument flexures, the differential refraction is responsible for shifts between each step image of the scan. The correction is made by computing the maximum of the intercorrelation function, calculated between each image of the scan and a reference image, which is one of these. Because information on the edge of the images is lost after the recentering, it is important to choose the reference image in order to minimize the shifts that are applied.

3.2.5. Wavelength Calibration

The commands sent to the FP controller are BCVs, but the observer usually drives the interferometer with wavelengths, so a conversion function must be known. As introduced in

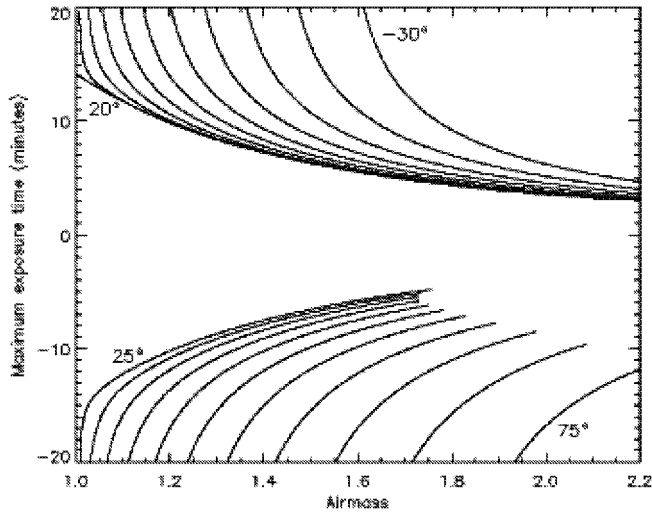


FIG. 14.—Maximum exposure time, as a function of the air mass, to prevent the differential refraction drift from being larger than one-fourth of the diffraction limit at $2.12 \mu\text{m}$. Atmospheric parameters are $T = 2^\circ\text{C}$, $P = 456 \text{ mm Hg}$. The negligible effect of water vapor has been ignored. The effective wavelength of sensing being unknown, we have taken a lower limit value of $0.6 \mu\text{m}$, which leads to the least favorable exposure time values. Each line corresponds to a different object declination, from -30° to $+75^\circ$. For a clearer presentation, maximum exposure time values calculated for declinations greater than the CFHT latitude ($19^\circ 49' 41'' 86$) have been negated.

§ 3.1.1, a calibrated emission line is scanned for this purpose. Each step image of the scan is averaged to construct the profile as a function of BCV. A Gaussian or Lorentzian fit is applied to know for which BCV the emission peaks. This value and the corresponding calibrated emission wavelengths are then set as parameters of the interferometer control software.

This calibration scan has a second utility. It is used to compute a so-called phase map that describes the wavelength correction variation along the field of the camera: from this scan, we build a map that indicates, for each pixel, the difference between the step number at which the emission is maximum and the expected step number at which this maximum should have occurred. The process followed to obtain this map is the same as the one used to derive the “conversion parameters” above, except that it is done for each pixel and not on the mean values of the scan.

During our first GriF run, two Gumball argon lamps were used to scan the $2.06163 \mu\text{m}$ line. The scanning step size, equal to $4.21 \times 10^{-4} \mu\text{m}$ in our case, i.e., around four-tenths of the instrumental resolution, must be chosen to correctly sample the instrumental profile.

The wavelength correction may differ according to two situations, as follows.

- The “conversion parameters” are entered in the software between the calibration and the scientific scans. The adjustment is not the same for the two scans. To obtain the

phase map to be used for the wavelength correction, one has to consider the original phase map and subtract from it its median value.

- The two scans (calibration and scientific) are done after the conversion parameters are entered. Both scans have the same wavelength adjustment, and this phase map can be directly used to make the wavelength correction.

To know the wavelength corresponding to a given pixel, for a given step image, one has to multiply the phase map value of this pixel by the scanning step size, in order to have a value expressed in wavelength. Next, one has to subtract the obtained value from the wavelength requested to the CS 100 for this image: this is the wavelength correction.

3.2.6. Atmospheric Contributions

Scientific spectra are polluted by the airglow emission and the telluric absorption features. The latter originates from rotational and vibrational states of OH and H_2O molecules. The infrared sky spectrum contains a huge amount of emission lines that are superposed on the scientific measurements. To remove these features, one has to obtain a sky spectrum having the same characteristics as the object spectra: same wavelength domain and same exposure time. An alternative solution could be to extract this spectrum from one or several spatial regions of the scientific cube showing no emission in the studied lines. The sky spectrum is then subtracted from the scientific one.

To correct from the telluric features, one has to observe a source known for its flat featureless spectrum, such as some A0 stars. The observed wavelengths must be the same as for the scientific cube. Spectra corrected from the airglow emission must then be divided by this calibration spectrum to obtain the final data.

4. FIRST GriF OBSERVATIONS IN FABRY-PÉROT SCANNING MODE

4.1. The OMC-1 Region

At a distance of 450 pc, the Orion molecular cloud (OMC-1) is the nearest star-forming region. When interacting with the ambient molecular cloud, the important outflows involved in the star-forming process give rise to shocks revealed by the infrared H_2 emission (Gautier et al. 1976). The complex finger-like structure of this emission was first described by Taylor et al. (1984) and was later found to be associated with Herbig-Haro objects (Allen & Burton 1993) probably ejected from a source near the Becklin-Neugebauer (BN) and IRC2 objects (Jones & Walker 1985).

After the first historical observations made by Matsumoto, Moritsugu, & Uyama (1985), two infrared three-dimensional spectroscopic programs (Chrysostomou et al. 1997; Salas et al. 1999), with their high spectral resolution (14 km s^{-1} for the former, 24 km s^{-1} for the latter), made it possible to spectrally

resolve the H_2 (1–0) $S(1)$ line emission. Broad profiles were found to have a central velocity fairly constant over the region, except for some blueshifted filaments. However, these data suffer from poor spatial resolution, between 1"5 and 2". Despite a marginally insufficient spectral resolution, which is still much better than usual interference filters, GriF can put its near diffraction limit capabilities to good use. Excellent spatial resolution is mandatory to avoid confusion and precisely assign the derived velocities to the observed structures, without any spatial averaging effect.

4.2. Observations

GriF's first astronomical observations in FP scanning mode were obtained on 2000 December 5. They were made during the observing run of Jean-Louis Lemaire and David Field. Four fields around the BN and Irc2 objects within OMC-1 have been successively scanned in the H_2 $v = 1-0$ $S(1)$ emission line at 2.12 μm .

In the following, the observed regions will be numbered 1–4. The central positions of each one, with respect to BN, are as follows: region 1, 15" south and 30" east; region 2, 15" south and 10" west; region 3, 15" north and 10" east; and region 4, 15" north and 30" west.

For the first two regions, the adaptive optics system was servoed on TCC 16, a 12 mag variable star. This star is located in region 1, 15" south and 10" east from BN. The reference star used for Region 3 is Parenago 1838, an 8 mag star. Parenago 1819, a 12 mag star, was used to servo the adaptive optics system for the last region.

To prevent the superposition of several FP orders, we inserted between the FP and the detector the usual CFHT H_2 $v = 1-0$ $S(1)$ interference filter, with a 2.122 μm central wavelength and a bandwidth of 0.020 μm .

Table 4 gives the wavelengths that we sent to the controller. Note that they are not the "real" wavelengths since they must be corrected from the instrumental response and from wavelength shifts that might occur with the varying position of the telescope (cf. § 3.2). FP scans have been made with a step size from 4.4×10^{-4} to 4.6×10^{-4} μm (i.e., around 65 km s^{-1}), allowing the correct sampling of the instrumental profile. For each wavelength and each region, a single exposure was done, with an integration of 400 s (300 for the first two wavelengths of region 1).

Between these object scans, flat-field and wavelength calibration cubes were built by scanning a halogen lamp (providing the flat spectrum) for the former and a calibrated argon lamp for the latter (cf. § 3.2).

4.3. Results

Figure 15 presents the "velocity map" of the first observed region. The others will be presented and discussed in a forthcoming paper. The velocity map indicates, for each pixel of the field, the wavelength for which the H_2 (1–0) $S(1)$ emission

TABLE 4
REQUESTED WAVELENGTHS TO BE SCANNED
FOR EACH REGION

Region 1 (μm)	Region 2 (μm)	Region 3 (μm)	Region 4 (μm)
2.1194	2.1186	2.1186	2.1186
2.120467	2.119036	2.119036	2.119036
2.121	2.119857	2.119473	2.119473
2.121457	2.120314	2.119909	2.119909
2.121533	2.120771	2.120345	2.120345
2.121914	2.121229	2.120782	2.120782
2.122371	2.121686	2.121218	2.121218
2.1226	2.122143	2.121655	2.121655
2.122829	2.1226		2.122091
2.123286			2.122527
2.123743			
2.1242			

is maximum. Values have been obtained by Lorentzian or Gaussian fit of each pixel profile. The black color corresponds to pixels where only a continuum emission has been detected.

With respect to the GriF spectral resolution, the 3.8 km s^{-1} heliocentric velocity component of the Earth at the observing date can be neglected and local standard of rest velocities can be directly computed by using the 2.12125 μm laboratory emission wavelength. Hence, the [2.1205 μm , 2.1212 μm] wavelength range of the figure corresponds to local standard of rest velocities between -106 and -7 km s^{-1} .

Two spectra have been extracted from region 1 (Fig. 16). One corresponds to a pixel in the central elliptical red region of Figure 15, whereas the other was taken from a pixel in the arch-shaped blue structure at the right of the same figure. These spectra demonstrate that even if the range of velocities encountered (-106 to -7 km s^{-1}) is smaller than the instrumental width, profile fitting allows one to improve considerably the actual velocity resolution of the instrument: the velocity difference between these two spectra is 80 km s^{-1} .

The stability of the absolute wavelength calibration can be estimated by

- knowing that in order to have homogeneous results in adjacent regions, values of region 2 have been translated with a value of 0.0002 μm (28 km s^{-1}) and values of region 3 have been translated with a value of -0.0002 μm (-28 km s^{-1}). These values are much smaller than the instrumental resolution (150 km s^{-1}) and give an estimation for the precision of the velocity measurements.
- Comparing values in the common fields between regions 1 and 2, regions 1 and 3, and regions 2 and 4.

Scientific results from these OMC-1 observations will be discussed in a following paper.

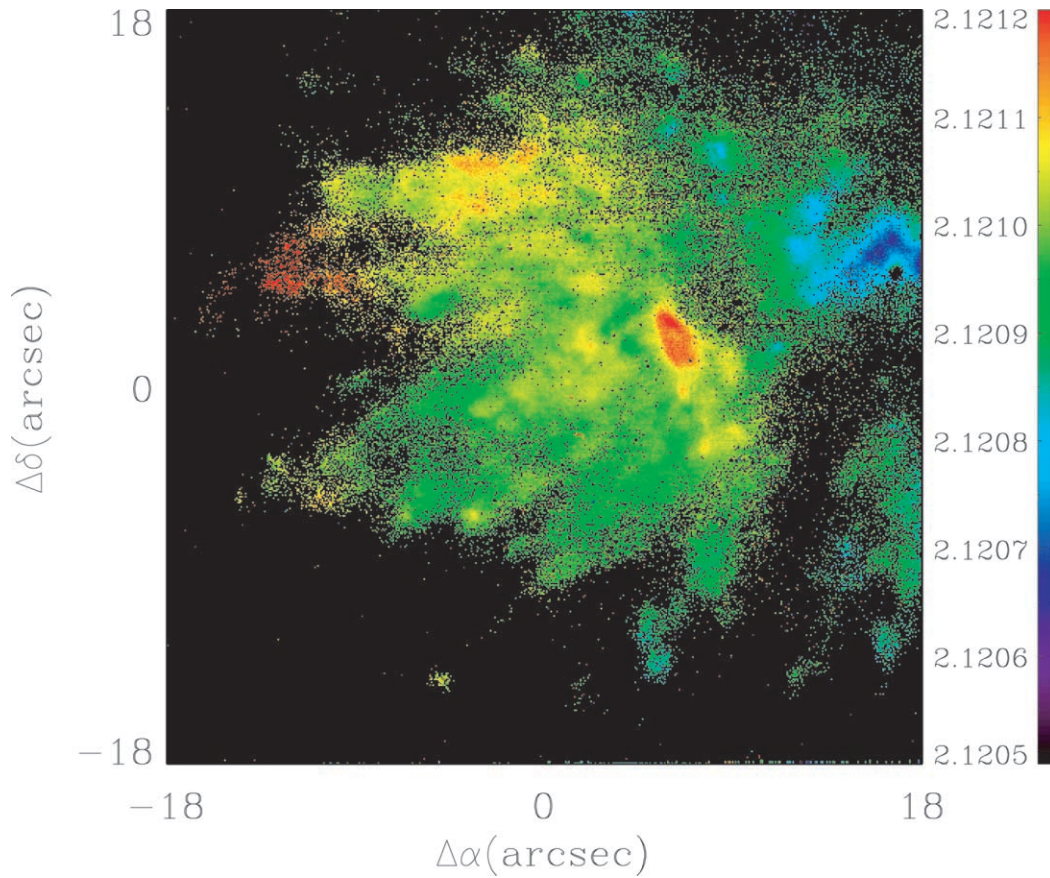


FIG. 15.—H₂ (1–0) S(1) velocity map of region 1. Data are not expressed in velocity units as in classical velocity maps but in detected wavelengths for which the emission is maximum. Black corresponds to continuum regions of the field where no significant variation of emission has been detected.

5. CONCLUSION

We have described in this article the instrumental setup of GrIF. Installed at the output of PUEO, the CFHT adaptive optics bonnette, this new instrument, which associates an FP interferometer with a cold grism, offers new infrared spectroscopic and three-dimensional observing modes. Hence, it combines imaging at diffraction limit with spectroscopic capabilities at a 2000 spectral resolution.

GrIF can be dedicated to a large range of scientific programs thanks to

- the outstanding performances reached by PUEO, notably in terms of limiting magnitude of the reference star for the wave front sensing;
- the much lower absorption by the interstellar medium in the near-infrared domain compared to the visible wavelengths, where opacity can be a very limiting factor, especially for compact objects where dust is often highly concentrated (protostars, young stellar objects, circumstellar envelopes around asymptotic giant branch [AGB] and post-AGB stars, starbursters, active galactic nuclei, etc.); and

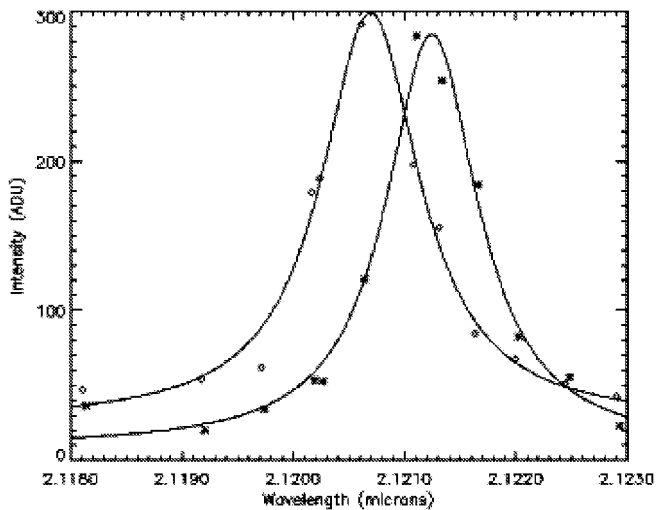


FIG. 16.—Two extracted spectra of region 1. Discrete values are pixel intensities taken from each step image. Lines are Lorentzian fits.

- the *K*-band richness in spectroscopic signatures of molecules, atoms, ions, and solids that give direct physical information on stellar population, the interstellar medium, or planet atmospheres or surfaces. In the case of the interstellar medium, important features are the quadrupolar lines of molecular hydrogen [$\text{H}_2 v = 1-0 S(1), \dots$] and the Brackett γ line tracing ionized hydrogen. Regarding the stellar population, the CO band head (2.3–2.4 μm), indicative of giants and supergiants, and the helium line at 2.058 μm are among the most important ones. Atmospheres and mineral surfaces of objects in the solar system can also be probed in lines or bands such as those of methane (2.0 μm) or broad organic bands such as those at 2.07 and 2.27 μm .

The first observations performed in FP scanning mode have demonstrated that a much higher velocity precision than the

150 km s^{-1} FP instrumental resolution can be reached. Compared with its parent project, GraF, GriF has a much better sensitivity but is still affected by an inconvenience due to its spectral resolution and the small pixel size of KIR: the sky noise limit can be reached only for rather bright objects. This limiting factor will be overcome only by improving the readout noise of infrared arrays.

Already available to the scientific community in shared risk mode, GriF will be completed by the end of 2001. A possible extension in the *H* band by using an additional grism is contemplated.

The GriF team would like to warmly thank Jean-Louis Lemaire, from Observatoire de Paris (France), and David Field, from the University of Aarhus (Denmark), since they gave us the opportunity to use GriF for the first time during one of their allocated nights.

REFERENCES

- Allen, D. A., & Burton, M. G. 1993, *Nature*, 363, 54
- Chalabaev, A., Le Coarer, E., Rabou, P., Mignart, Y., Petmetsakis, P., & Le Mignant, D. 1999, in *ESO Conf. Proc. 56, Astronomy with Adaptive Optics: Present Results and Future Programs*, ed. D. Bonaccini (Garching: ESO), 61
- Chrysostomou, A., Burton, M. G., Axon, D. J., Brand, P. W. J. L., Hough, J. H., Bland-Hawthorn, J., & Geballe, T. R. 1997, *MNRAS*, 289, 605
- Cohen, J. G., & Cromer, J. 1988, *PASP*, 100, 1582
- Davies, R. I., Kasper, M. E., Thatte, N. A., Tecza, M., Tacconi-Garman, L. E., Anders, S. W., & Herbst, T. 2000, *Proc. SPIE*, 4007, 952
- Doyon, R., Nadeau, D., Vallée, P., Starr, B. M., Cuillandre, J. C., Beuzit, J.-L., Beigbeder, F., & Brau-Nogue, S. 1998, *Proc. SPIE*, 3354, 760
- Fabry, C. 1905, *CR Acad. Sci. Paris*, 140, 848
- Fabry, C., & Pérot, A. 1901, *ApJ*, 13, 265
- Filippenko, A. V. 1982, *PASP*, 94, 715
- Gautier, T. N., Fink, U., Treffers, R. R., & Larson, H. P. 1976, *ApJ*, 207, L129
- Jones, B. F., & Walker, M. F. 1985, *AJ*, 90, 1320
- Kern, P., Rigaut, F., Léna, P., Merkle, F., & Rousset, G. 1990, *Proc. SPIE*, 1237, 345
- Mandel, H., et al. 2000, *Proc. SPIE*, 4008, 767
- Matsumoto, T., Moritsugu, T., & Uyama, K. 1985, *PASJ*, 37, 129
- McGregor, P. J., Conroy, P., Bloxham, G., & Van Harmelen, J. 1999, *Publ. Astron. Soc. Australia*, 16, 273
- Mengel, S., Eisenhauer, F., Tecza, M., Thatte, N. A., Roehrl, C., Bickert, K., & Schreiber, J. 2000, *Proc. SPIE*, 4005, 301
- Murray, G. J., Allington-Smith, J. R., Content, R., Dodsworth, G. N., Dunlop, C. N., Haynes, R., Sharples, R. M., & Webster, J. 2000, *Proc. SPIE*, 4008, 611
- Pietraszewski, K. A. R. B. 2001, in *ASP Conf. Ser. 195, Imaging the Universe in Three Dimensions*, ed. W. van Breugel & J. Bland-Hawthorn (San Francisco: ASP), 591
- Rigaut, F., et al. 1998, *PASP*, 110, 152
- Salas, L., et al. 1999, *ApJ*, 511, 822
- Taylor, K. N. R., Storey, J. W. V., Sandell, G., Williams, P. M., & Zealey, W. J. 1984, *Nature*, 311, 236